Available online at www.sciencedirect.com

SciVerse ScienceDirect

Ceramics International 39 (2013) 5597–5608

CERAMICS INTERNATIONAL

www.elsevier.com/locate/ceramint

Optical, photocatalytic and bactericidal properties of $Zn_{1-x}La_xO$ and $Zn_{1-x}Mg_xO$ nanostructures prepared by a sol–gel method

Sumetha Suwanboon[a,e,*], Pongsaton Amornpitoksuk[b,e], Phuwadol Bangrak[c], Nantakan Muensit[d,e]

[a]*Department of Materials Science and Technology, Faculty of Science, Prince of Songkla University, Hat Yai, Songkhla 90112, Thailand*
[b]*Department of Chemistry and Center of Excellence for Innovation in Chemistry, Faculty of Science, Prince of Songkla University, Hat Yai, Songkhla 90112, Thailand*
[c]*School of Science, Walailak University, Nakhon Si Thammarat 80161, Thailand*
[d]*Department of Physics, Faculty of Science, Prince of Songkla University, Hat Yai, Songkhla 90112, Thailand*
[e]*Center of Excellence in Nanotechnology for Energy (CENE), Prince of Songkla University, Hat Yai, Songkhla 90112, Thailand*

Received 18 October 2012; received in revised form 13 December 2012; accepted 19 December 2012
Available online 9 January 2013

Abstract

Multifunctional $Zn_{1-x}La_xO$ and $Zn_{1-x}Mg_xO$ nanostructures were successfully synthesized through a sol–gel method. The crystal structure, morphology, specific surface area and thermal behavior were investigated by X-ray diffractometer (XRD), scanning electron microscopy (SEM), transmission electron microscopy (TEM), Brunauer–Emmett–Teller (BET) and a thermogravimetric and differential thermal analyzer (TG–DTA), respectively. The optical properties were determined with a UV–vis spectrophotometer and a photoluminescent spectrometer. The crystallite size decreased when the La and Mg concentrations increased to $x=0.05$. The $Zn_{0.9}Mg_{0.1}O$ nanostructure showed the widest E_g value of 3.30 eV. The $Zn_{0.95}Mg_{0.05}O$ nanostructure exhibited the highest efficiency for the photocatalytic degradation of methylene blue (MB) with a rate constant (k) of 0.0440 min^{-1}. Both La- and Mg-doped ZnO nanostructures inhibited *Staphylococcus aureus* (*S. aureus*) and to a less extent *Escherichia coli* (*E. coli*).

Keywords: A. Sol–gel processes; C. Optical properties; D. ZnO; E. Functional applications

1. Introduction

Zinc oxide (ZnO) is a natural *n*-type II–VI semiconductor because it has deviations from stoichiometry due to the presence of intrinsic defects such as oxygen vacancies and zinc interstitials [1]. ZnO is a superior multifunctional material with broad applications in electronics [2], optoelectronics [3], dielectrics [3], sensing materials [3], as a photocatalyst [4] and as an antimicrobial agent [5]. Recently, many research groups have been interested in the synthesis of ZnO nanostructures using wet chemical methods such as precipitation [6], hydrothermal [7] and sol–gel [8]. Among the wet chemical methods, sol–gel is perhaps the major method used to prepare ZnO nanostructures because this method has many advantages [9] such as (1) it requires a low temperature, (2) doping with other metals is straightforward, (3) nanocrystalline products can be prepared and (4) the structure of the product can be pre-determined by varying the experimental conditions such as by the use of a capping agent, or a change in pH and temperature. As a photocatalyst and antimicrobial agent, ZnO and metal-doped ZnO nanostructures have attracted interest because of their ability to be used for the remediation of certain environmental pollutants. Research has focused on its photocatalytic activities, for which the electrons in the valence band gain photon energy that is higher than its bandgap energy, so electrons are excited to conduction bands and holes are generated in the valence band. After being photo-excited, electrons and holes move

*Corresponding author at: Department of Materials Science and Technology, Faculty of Science, Prince of Songkla University, Hat Yai, Songkhla 90112, Thailand. Tel.: +66 7428 8385; fax: +66 7428 8395.
E-mail address: ssuwanboon@yahoo.com (S. Suwanboon).

0272-8842/$ - see front matter © 2013 Elsevier Ltd and Techna Group S.r.l. All rights reserved.
http://dx.doi.org/10.1016/j.ceramint.2012.12.075

to the surface of the catalyst where if there is water and oxygen, the super-oxide anion radicals ($\bullet O_2^-$) and hydroxyl ($\bullet OH$) radicals are produced, and these degrade organic compounds [10]. In order to enhance the photocatalytic activity, the influence of various doping metals such as Ag, Co, Mn, Mg and Cu on the photocatalytic degradation of dyes has been investigated [10–13]. The doping metals incorporated into the ZnO lattice can either increase or decrease the efficiency of the photocatalytic degradation that is dependent on many key parameters such as the specific surface area, defects and the retardation of recombination of the photo-excited electrons and holes [10–13]. Recently, the influence of metal-doped ZnO nanostructures on its antimicrobial activity has been a major area of investigation because microbial contamination is a serious problem in healthcare. The antimicrobial activity has been tested by various methods. Nirmal and Anukaliani [14] reported that Co-doped ZnO powders had enhanced antibacterial activity and Co-doped ZnO powders exhibited excellent antibacterial activity towards *Staphylococcus aureus* (*S. aureus*). Ghosh et al. [15] investigated the influence of Ag in a ZnO/Ag nanohybrid and they found that Ag improved the antibacterial activity against *S. aureus* and *Escherichia coli* (*E. coli*). Moreover, Karunakaran et al. [16] also reported that Ag-doped ZnO particles had enhanced antibacterial activity whereas Amornpitoksuk et al. [17] showed that Ag-doped ZnO powders were more effective against *S. aureus* than *E. coli* and the best antibacterial activity toward *S. aureus* was 0.5–0.8 mol% Ag, but the Ag concentration did not affect the inhibition of *E. coli*. Rekha et al. [18] reported that Mn-doped ZnO powders had better antibacterial activity than pure ZnO powders. Recently, the mechanism of antibacterial activity has mostly focused on the physical attack of nanoparticles on bacteria. However there have been no publications on the influence of La- and Mg-doped ZnO nanostructures prepared from poly(ethylene oxide)-b-poly(propylene oxide)-b-poly(ethylene oxide)-modified $Zn(CH_3COO)_2 \cdot 2H_2O$ solution by the sol–gel method. In this study, the effects of doping with La and Mg on the ZnO and the optical, photocatalytic and antibacterial properties were investigated.

2. Experimental

2.1. Materials

Zinc acetate dihydrate ($Zn(CH_3COO)_2 \cdot 2H_2O$) (Analytical grade, Fluka, Germany), lanthanum chloride hydrate ($LaCl_3 \cdot H_2O$) (Analytical grade, Fluka, Germany), magnesium chloride hexahydrate ($MgCl_2 \cdot 6H_2O$) (Analytical grade, Merck, Germany) were used as the zinc, lanthanum and magnesium sources, respectively. Poly(ethylene oxide)-b-poly(propylene oxide)-b-poly(ethylene oxide) (PEO_{128}–PPO_{54}–PEO_{128}, MW 14,400) (Analytical grade, Fluka, USA) was used as a capping agent. Anhydrous sodium carbonate (Na_2CO_3) (Analytical grade, Riedel-de Haën, Germany) was used as a precipitating agent. Methylene blue ($C_{16}H_{18}N_3CIS \cdot 2H_2O$) (Analytical grade, NILAB, Australia) was used as a representative dye. All chemicals were used without further purification.

2.2. Preparation of $Zn_{1-x}La_xO$ and $Zn_{1-x}Mg_xO$ nanostructures

In order to investigate the effect of La and Mg concentrations on the properties of the ZnO nanostructure, the stoichiometric amounts of $LaCl_3 \cdot H_2O$ and $MgCl_2 \cdot 6H_2O$ were added separately into 100 mL of a PEO_{128}–PPO_{54}-PEO_{128}-assisted $Zn(CH_3COO)_2 \cdot 2H_2O$ solution to obtain $Zn_{1-x}La_xO$ or $Zn_{1-x}Mg_xO$ (x=0.01, 0.03, 0.05, 0.07 and 0.10). The Na_2CO_3 solution (10.60 g Na_2CO_3 in 100 mL of distilled H_2O) was then added slowly into the above solutions with vigorous stirring. A gel was formed during the addition of the Na_2CO_3 solution and the obtained gel was continuously stirred at 60 °C for 1 h. After being cooled to room temperature, the solvent was removed by filtration and the gel was then dried at room temperature until a xerogel was obtained. The xerogel was ground into a fine powder using an agate mortar, in addition, the powder was then calcined at 600 °C in air for 1 h to remove the organic compounds. The products were slowly cooled to room temperature in the furnace and the nanostructures of the La- and Mg-doped ZnO were determined. The procedure for the preparation of nanostructures is represented in Fig. 1.

2.3. Characterization

The thermal characteristics of the xerogel were studied using the thermogravimetric analyzer (TGA7, Perkin Elmer) and differential thermal analyzer (DTA7, Perkin Elmer) in the temperature range of 50–900 °C at a heating rate of 10 °C/min under a nitrogen flux. The crystal

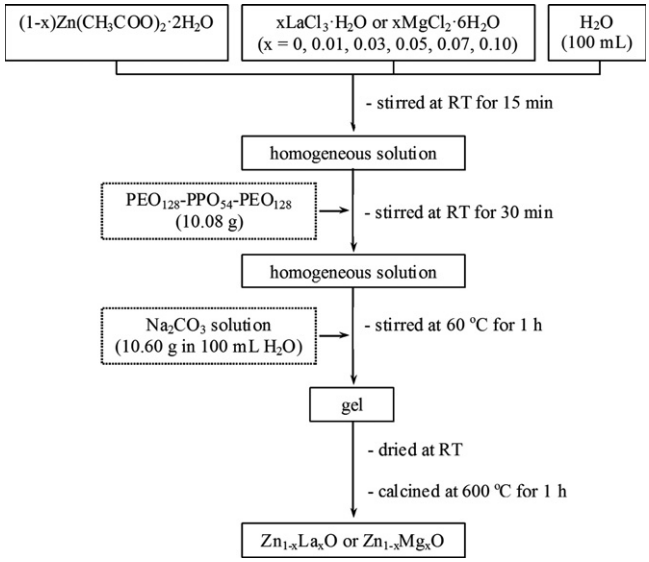

Fig. 1. Representation of the preparation of the products by a sol–gel technique.

structure of the samples was characterized by X-ray diffractometer (X'Pert MPD, Philips) with CuK_α radiation in the 2θ range of 20–80°. The morphology of the samples was characterized by scanning electron microscopy (SEM, QUANTA 400, FEI) and transmission electron microscopy (TEM, JEM-2010, JEOL). The diffuse reflectance spectra of the samples were recorded by a UV–vis spectrophotometer (UV–vis 2450, Shimadzu). The room temperature photoluminescence (PL) spectra were measured using a luminescence spectrometer (LS/55, Perkin Elmer). The total surface area of the samples was determined by the Brunauer–Emmett–Teller (BET) method using the surface area analyzer (Autosorb 1 MP, Quantachrome).

2.4. Measurement of photocatalytic activity

The photocatalytic activities of $Zn_{1-x}La_xO$ or $Zn_{1-x}Mg_xO$ (x=0, 0.05 and 0.10) nanostructures were evaluated by the degradation of an aqueous MB solution. The photocatalytic reaction system consisted of three Blacklight Blue lamps (18 W, Sylvania) located 15 cm away from the top of the reaction solution. 150 mg of each catalyst was put into 150 mL of the aqueous MB solution at a concentration of 1×10^{-5} M in a 250 mL beaker and the suspension was stirred for 30 min in the dark to attain an equilibrium of the adsorption–desorption process. After each given irradiation time (30 min), 3 mL of suspension was kept and separated by centrifuging for 2 min at a speed of 3000 rpm to remove the catalyst. The degradation process was followed by measuring the absorbance of the supernatant or the aqueous MB solution left, with a UV–vis spectrometer (Lamda 25, Perkin Elmer).

2.5. Determination of antibacterial activity

The minimum inhibitory concentration (MIC) of representative samples was determined by a broth microdilution method [19]. *S. aureus* ATCC 25923 and *E. coli* ATCC 25922 were used as representative microorganisms for Gram-positive and Gram-negative bacteria, respectively. In order to examine the antibacterial activity of the representative samples, $Zn_{1-x}La_xO$ or $Zn_{1-x}Mg_xO$ (x=0, 0.05 and 0.10) nanostructures were suspended in sterile distilled water and sonicated for 20 min to yield a stock solution of 50 mg/mL and the representative samples were diluted using the two-fold serial dilution method starting with 50 and diluting to 0.78 mg/mL. The bacterial suspensions were prepared in normal saline solution (NSS) with an optical density equivalent to the 0.5 McFarland standard, and diluted to 1:20 in NSS to obtain a final concentration of about 5×10^6 CFU/mL. Then triplicate 50 μL samples of each dilution were applied into a sterile 96-well microtiter plate. To each well was added 10 μL of 0.675% (w/v) resazurin solution as an indicator and 30 μL of 3.3 strength Mueller Hinton Broth (3.3 × MHB). Finally, 10 μL of bacterial suspension (5×10^6 CFU/mL) was applied to achieve a concentration of 5×10^5 CFU/mL. The microtiter plates were prepared in triplicate. After incubation at 30 °C for 20 h, the lowest concentration at which no color change occurred was taken as the MIC value.

3. Results and discussion

3.1. Thermal study

The TGA and DTA curves of the ZnO xerogel are shown in Fig. 2. Three weight loss steps were observed in the TGA curve at about 50–180, 180–280 and 280–530 °C and two large endothermic as well as small endothermic peaks were observed in the DTA curve at about 100, 212 and 326 °C. The first endothermic peak was attributed to an evaporation of the adsorbed water from the xerogel and was accompanied by a weight loss of about 25%. The second and third endothermic peaks were caused by the dehydration of the crystallized water and the decomposition of the PEO_{128}–PPO_{54}–PEO_{128} and other organic molecules [20] accompanied by a weight loss of about 19%. It was evident that no other weight losses in the TGA curve were observed at temperatures higher than 550 °C. Therefore, the xerogel had to be calcined at 600 °C in order to burn out any organic or other undesirable residues.

3.2. Structural study

The typical XRD patterns of $Zn_{1-x}La_xO$ and $Zn_{1-x}Mg_xO$ (x=0–0.10) nanostructures calcined at 600 °C for 1 h are presented in Fig. 3. Obviously, the diffraction peaks of $Zn_{1-x}La_xO$ and $Zn_{1-x}Mg_xO$ nanostructures can be indexed to the hexagonal wurtzite structure in agreement with the diffraction pattern of the ZnO standard (JCPDS card number of 36-1451).

To investigate the effect of La and Mg concentrations on the crystallinity, the crystallite size of the samples was evaluated by measuring the broadening of the XRD peaks

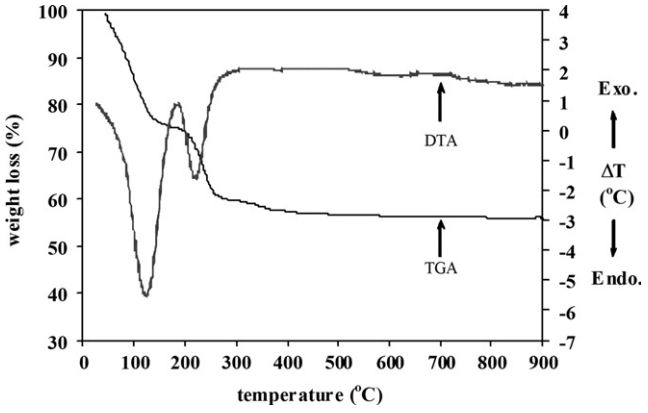

Fig. 2. TG–DTA curves of the ZnO xerogel at a specified heating rate of 10 °C/min.

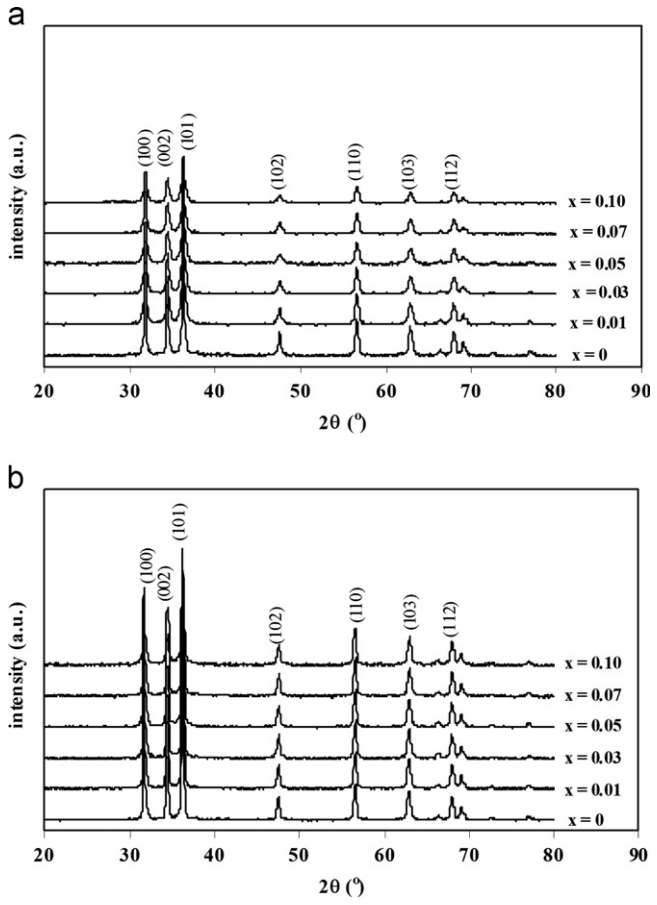

Fig. 3. XRD patterns of the calcined nanostructures (a) $Zn_{1-x}La_xO$ and (b) $Zn_{1-x}Mg_xO$.

using the Scherrer formula [21]:

$$D = \left(\frac{180}{\pi}\right)\left(\frac{K\lambda}{\cos\theta\sqrt{\beta^2 - s^2}}\right) \quad (1)$$

where D is the crystallite size, λ is the wavelength of the CuK_α radiation (0.15406 nm), K is a constant (0.9), s is the instrumental broadening, β is the full-width at half-maximum and θ is the Bragg angle. The calculated crystallite size is given in Table 1. In this study, the lattice parameters a and c of the calcined samples were calculated via the relation below [22] and the results are presented in Table 1.

$$\sin^2\theta = \frac{\lambda^2}{4}\left[\frac{4}{3}\left(\frac{h^2 + hk + k^2}{a^2}\right) + \frac{l^2}{c^2}\right] \quad (2)$$

where θ is the Bragg angle, λ is the wavelength of the CuK_α radiation (0.15406 nm) and h, k, l are Miller indices. Furthermore, the lattice volume was also evaluated by the formula below [23]:

$$V = 0.866a^2c \quad (3)$$

where V is the lattice volume, a and c are the lattice constant. The calculated results are presented in Table 1.

The effects of the La and Mg concentrations on the lattice parameters are presented in Table 1. Theoretically, the substitutional solid solution can form easily if the solute and solvent atoms obey these conditions: (1) the difference in the ionic radius was not more than 15%, (2) the crystal structure of the solute and solvent atoms were the same, (3) the electronegativity of the solute atom was close to the solvent atom and (4) the valency was the same [24]. The ionic radius of La^{3+} (116 pm) was much larger than the ionic radius of Zn^{2+} (74 pm) with a valency difference of 1. Thus, it is very difficult for the La^{3+} ions to substitute for the Zn^{2+}. This is in good agreement with the lattice parameters of the La-doped ZnO nanostructures obtained in Table 1. It is well known that the lattice parameters of ZnO have to expand if the La^{3+} ions, that have a larger ionic radius, were to substitute at the Zn^{2+} sites in the ZnO lattice, but the lattice parameters of the La-doped ZnO nanostructures were contracted when compared with the pure ZnO nanostructures. Therefore, it can be concluded that the La^{3+} ions might be interstitial in the ZnO lattice and these La^{3+} ions formed a La–O–Zn structure on the surface of the ZnO nanostructures as reported previously [25]. This caused a decrease in the lattice parameters of the La-doped ZnO nanostructures when the La concentration was varied over the range of $x=0$–0.05. With a further increase of the La concentration to $x=0.10$, the lattice parameter and the lattice volume increased. This is possibly due to the growth of a crystal [26]. For the Mg-doped ZnO nanostructure, the ionic radius of the Mg^{2+} (72 pm) was close to the ionic radius of the Zn^{2+} (74 pm). Moreover, the electronegativity of the Mg (1.31) was also closer to that of the Zn (1.65) than it was for the La (1.10) and in addition the valency was also equivalent. Therefore, the substitution of Mg^{2+} ion at the Zn^{2+} site can occur more easily than a substitution by a La^{3+} ion. With regard to Table 1, the lattice parameter a is almost constant except at $x=0.10$, when the lattice parameter a expanded again. This might be due to the presence of larger defects in the ZnO structure [27] and to crystal growth. This effect has also been observed in Al-doped ZnO powders [28]. The decrease in the lattice parameter c of the Mg-doped ZnO nanostructures indicated that the Mg^{2+} ion could substitute at the Zn^{2+} site and form a substitutional solid solution.

When the influence of the La and Mg concentrations on the crystallite size were determined (Table 1), the dependence of the crystallite size on the La and Mg concentrations can be explained by the Zener pinning effect. The crystallite size of La- and Mg-doped ZnO nanostructure was slightly diminished when the La and Mg concentrations were increased to $x=0.05$. This is due to the dopant obstructing the movement of boundaries, and giving rise to an inhibition of the overall growth. On the other hand, the crystallite size of ZnO increased when being doping with $x > 0.05$, and this was caused by the coarsening of the dopant with a higher critical size, resulting in the reduction of the pinning efficiency. Therefore, the crystallite size could grow again [6].

To study the effect of La and Mg concentrations on a change of morphology, the samples were characterized by

Table 1
The structural and optical properties of $Zn_{1-x}La_xO$ and $Zn_{1-x}Mg_xO$ nanostructures.

Dopant	Content (x)	D (nm)	Lattice parameters			V (nm)^3	E_g (eV)
			a (nm)	c (nm)	c/a		
La	0	32.91	0.3247(1)	0.5202(9)	1.6023	0.0475(1)	3.20
	0.01	30.38	0.3247(0)	0.5201(0)	1.6018	0.0474(9)	3.18
	0.03	29.78	0.3245(3)	0.5200(0)	1.6023	0.0474(3)	3.18
	0.05	25.10	0.3243(1)	0.5200(0)	1.6037	0.0473(6)	3.18
	0.07	28.47	0.3246(7)	0.5201(9)	1.6022	0.0474(9)	3.18
	0.10	29.78	0.3249(1)	0.5199(6)	1.6003	0.0475(4)	3.18
Mg	0	32.91	0.3247(1)	0.5202(9)	1.6023	0.0475(1)	3.20
	0.01	31.89	0.3246(8)	0.5200(0)	1.6016	0.0474(7)	3.21
	0.03	30.82	0.3246(7)	0.5198(1)	1.6010	0.0474(5)	3.23
	0.05	29.27	0.3247(3)	0.5197(4)	1.6005	0.0474(6)	3.27
	0.07	31.64	0.3246(5)	0.5192(9)	1.5995	0.0474(0)	3.25
	0.10	32.19	0.3249(3)	0.5193(8)	1.5984	0.0474(9)	3.30

SEM and the images are presented in Fig. 4. The La concentration did not affect the particle shape of ZnO because the La^{3+} cannot substitute at the Zn^{2+} sites as mentioned previously. However, the La concentration still affected the particle size. This evidence was in good agreement with the result of the crystallite size obtained from the XRD analysis. In this study, the agglomerated spherical particles formed over the whole range of the La concentrations used and the particle size of the pure ZnO nanostructure decreased from 65 nm to 25 nm when being doped with $x=0.05$ as clearly observed in Fig. 4(g and h). As mentioned previously, the La produced a La–O–Zn on the surface of the ZnO nanostructures. This can be attributed to a provocation of isotropic growth, caused by the formation of a spherically shaped La-doped ZnO nanostructure. When Mg was used as a dopant, the particle shape altered from spherical to a rod structure with a diameter of about 100 nm when ZnO was doped with $x=0.10$. It was of interest that, the Mg concentrations influenced the growth mechanism of the ZnO nanostructure. The particle shape changed from a spherical to a nanorod structure when the Mg concentrations were increased (Fig. 5). This change was also observed in the Ni-doped ZnO nanostructure [29]. In this investigation, when the Zn^{2+} ions were substituted by Mg^{2+} ions this predominantly affected the lattice parameter c compared with the lattice parameter a. This might provide the driving force for anisotropic growth, as the ZnO nanorod formed when being doped with Mg. Moreover, the formation of Mg-doped ZnO nanorods can be explained by the Pechini process due to the addition of the PEO_{128}–PPO_{54}–PEO_{128}. This perhaps could lead to an esterification reaction or form a chelation with zinc acetate by the formed ester. After the calcination process, the ZnO nanorods were formed [30,31].

3.3. Optical study

The optical bandgap energy (E_g) of the ZnO nanostructures is an important parameter that has to be considered for use in special applications. It was evident that the E_g value may be dependent on the particle size, particle shape or defects [28] and these parameters strongly depended upon the synthetic method of the ZnO nanostructures. In this study, the absorbance of samples was recorded and the E_g value of the samples was determined by the following relation [29]:

$$(\alpha E) = B\left(E - E_g\right)^m \tag{4}$$

where B is an energy-independent constant, E_g is the direct bandgap energy, α is the absorption coefficient, E is the photon energy and m is an index that characterizes the optical absorption process and it is theoretically equal to 2 and 1/2 for an indirect and direct transition, respectively.

In this study, the absorption coefficient (α) can be estimated by the following relationship [6]:

$$\alpha = \frac{A}{d'} \tag{5}$$

where A is the measured absorbance and d' is the cell thickness or sample thickness (0.4 cm) and the photon energy can be approximated by the following relationship [6]:

$$E = \frac{1240}{\lambda} \tag{6}$$

where λ is the wavelength in nanometers.

The $(\alpha E)^2$ versus E for all samples was plotted as shown in Fig. 6 and the E_g values are given in Table 1. For the La-doped ZnO nanostructures, the E_g values were almost the same even though the La concentrations increased. However, the E_g values of the La-doped ZnO nanostructure were smaller than the E_g value of the pure ZnO nanostructure. The decrease in the E_g value may be due to the increase in defects such as the oxygen vacancies and this was confirmed by the resultant PL spectra in Fig. 7. The oxygen vacancies can induce the formation of new recombination centers with a lower conduction band, that gives rise to a narrower E_g value [32]. For the Mg-doped ZnO nanostructures, in contrast, the E_g value increased

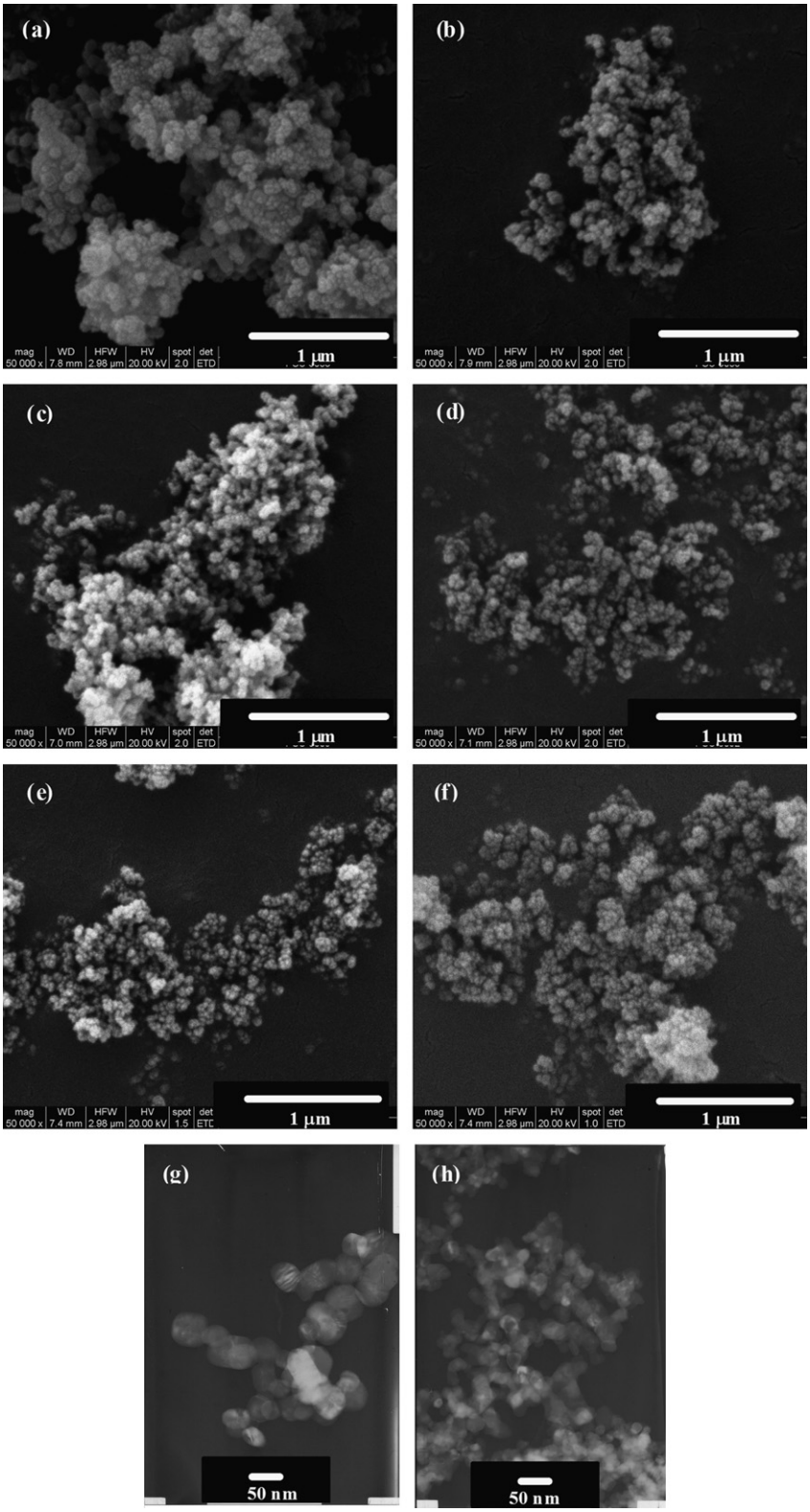

Fig. 4. SEM images of the calcined $Zn_{1-x}La_xO$ nanostructures at various La concentrations where (a) $x=0$, (b) $x=0.01$, (c) $x=0.03$, (d) $x=0.05$, (e) $x=0.07$ and (f) $x=0.10$ as well as the TEM images where (g) $x=0$ and (h) $x=0.05$.

systematically when the Mg concentrations were increased from $x=0$ to 0.05, and this might be due to the decrease in the crystallite size. When the Mg concentration was further increased to $x=0.07$, the E_g value decreased because of an increase in the crystallite size. However, the E_g value of $Zn_{0.90}Mg_{0.10}O$ increased again as there was then a complete change of the morphology [33]. This might be due to the formation of an amorphous MgO on the surface of the

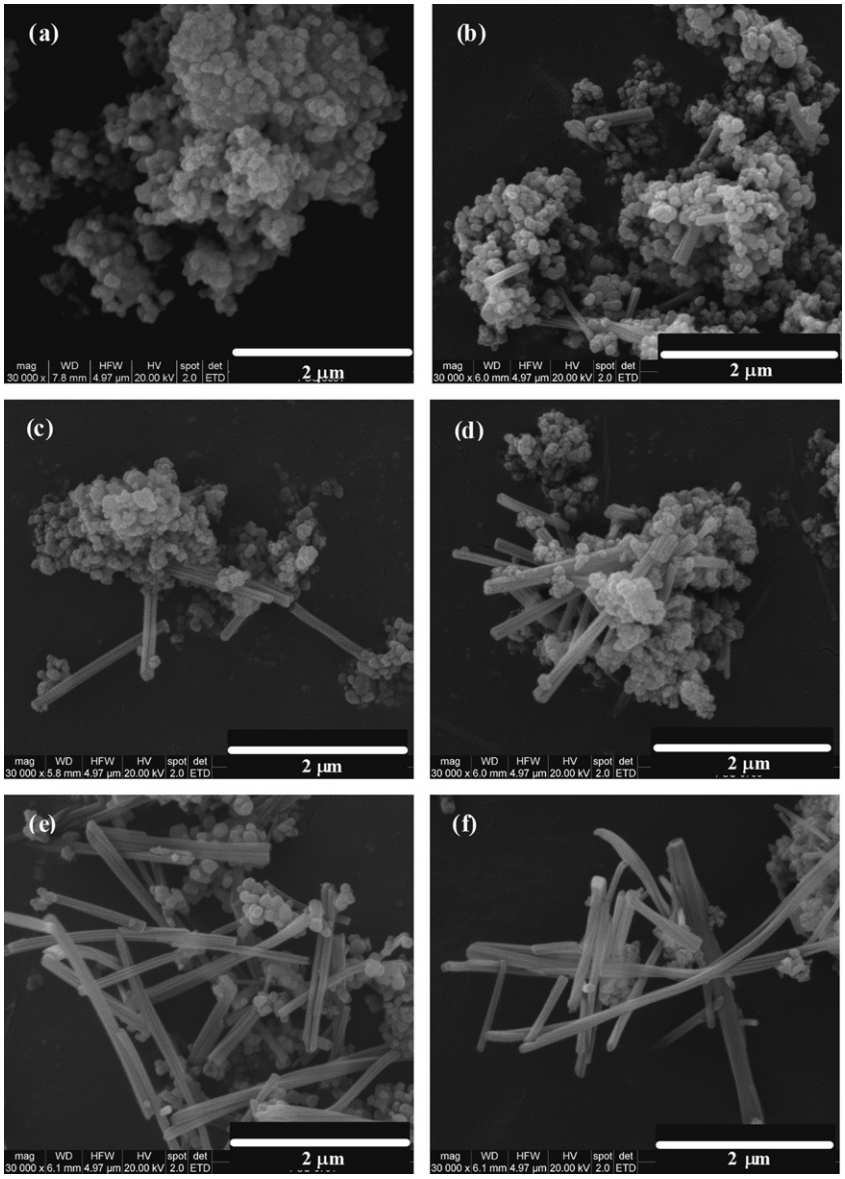

Fig. 5. SEM images of the calcined $Zn_{1-x}Mg_xO$ nanostructures at various Mg concentrations where (a) $x=0$, (b) $x=0.01$, (c) $x=0.03$, (d) $x=0.05$, (e) $x=0.07$ and (f) $x=0.10$.

catalyst and this MgO phase had a larger E_g value (5.4 eV) [12].

3.4. Photocatalytic activities

In this work, $Zn_{1-x}La_xO$ and $Zn_{1-x}Mg_xO$ ($x=0$, 0.05 and 0.10) were selected to be representative catalysts and an aqueous MB solution was used as the model pollutant with an initial concentration of 1×10^{-5} M. The evaluation of the photocatalytic activity was performed at ambient temperature and a pH of 6.5 under UV irradiation for different times.

Fig. 8 shows a temporal change of the absorption spectra of the aqueous MB solution in the presence of the ZnO catalyst. A decrease in the MB absorption at a wavelength of 664 nm was observed. This was due to the breaking of the conjugated chromophore structure of the MB [34]. Fig. 9(a) and (b) shows the efficiency of the photocatalytic degradation of the aqueous MB solution by the La and Mg-doped ZnO nanostructures. It was evident that the efficiency of photocatalytic degradation of the aqueous MB solution without any catalyst was almost constant over the whole range of irradiation times used. This indicated that the MB molecules were not degraded in the absence of catalyst. Therefore, it can be concluded that the photocatalytic property was activated by the catalysts in combination with the UV irradiation. In this study, it was observed that both La and Mg doping metals had enhanced photocatalytic activity. For the La-doped ZnO nanostructures, the efficiency of the photocatalytic degradation after UV irradiation for 1 h reached 83%, 93% and 90% for ZnO, $Zn_{0.95}La_{0.05}O$ and $Zn_{0.90}La_{0.10}O$, respectively.

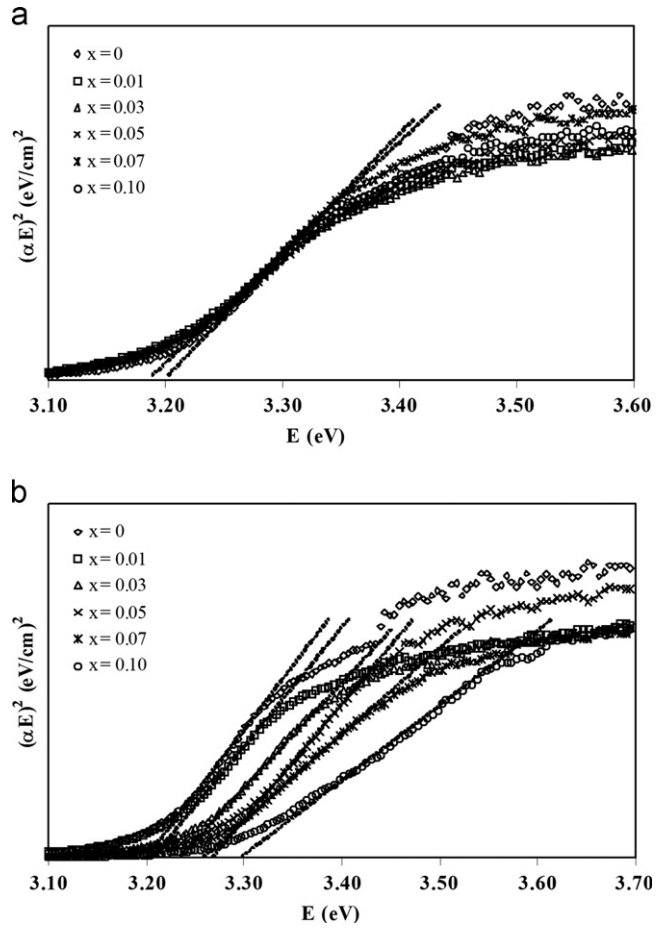

Fig. 6. Plots of $(\alpha E)^2$ versus E of (a) the $Zn_{1-x}La_xO$ nanostructures and (b) the $Zn_{1-x}Mg_xO$ nanostructures.

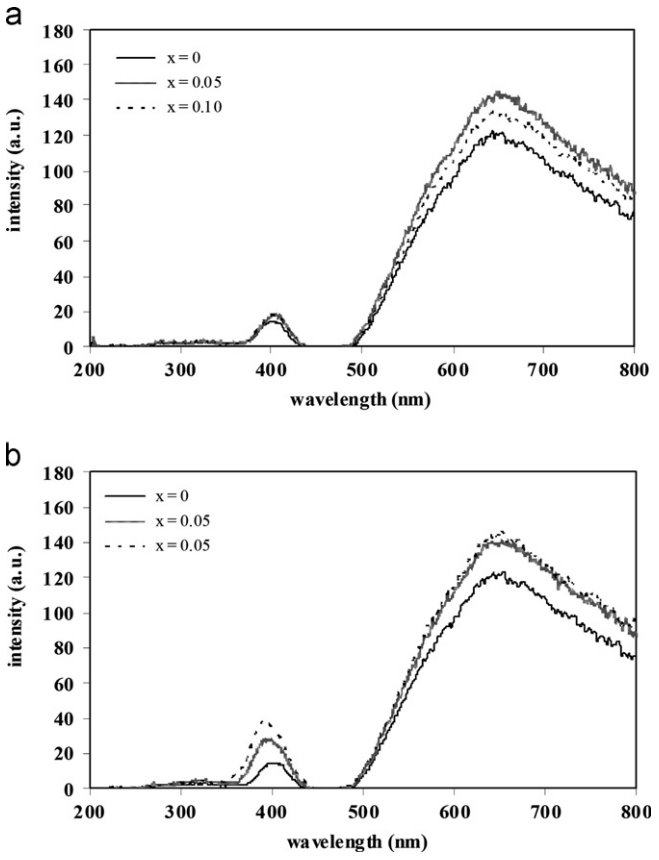

Fig. 7. Room temperature PL spectra of (a) the $Zn_{1-x}La_xO$ nanostructures and (b) the $Zn_{1-x}Mg_xO$ nanostructures.

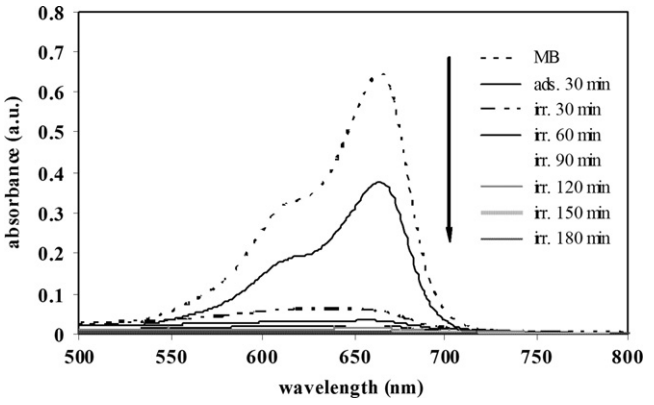

Fig. 8. The temporal change in the absorbance of the MB aqueous solution in the presence of the ZnO catalyst.

The efficiency of the photocatalytic degradation for ZnO, $Zn_{0.95}La_{0.05}O$ and $Zn_{0.90}La_{0.10}O$ nanostructures increased to 96% whereas the efficiency of the photocatalytic degradation of ZnO nanostructures reached 87% after UV irradiation for 2 h. When the Mg-doped ZnO nanostructure was used as a catalyst, the efficiency of photocatalytic degradation after UV irradiation for 1 h was about 83%, 92% and 88% for ZnO, $Zn_{0.95}Mg_{0.05}O$ and $Zn_{0.90}Mg_{0.10}O$, respectively. The MB degraded almost completely after UV irradiation for 2 h with an efficiency of photocatalytic degradation of about 99% and 98% for $Zn_{0.95}Mg_{0.05}O$ and $Zn_{0.90}Mg_{0.10}O$, respectively. It is well known that the photocatalytic activity is influenced by crystallinity, particle shape, defect concentrations and specific surface area [10–13]. In this study, the specific surface area of the representative catalysts was determined and the results are presented in Table 2. In the case of the La-doped ZnO nanostructures, the $Zn_{0.95}La_{0.05}O$ nanostructures had the highest specific surface area (29.89 m^2/g). This gave rise to the highest efficiency of photocatalytic degradation of the MB solution because the catalyst had the most active sites in the photocatalytic process. In addition the $Zn_{0.95}La_{0.05}O$ nanostructures had the biggest concentration of defects or oxygen vacancies and this also brought about an improvement of photocatalytic activity due to the catalyst having the most active centers [35]. For the Mg-doped ZnO nanostructures, the efficiency of the photocatalytic degradation of $Zn_{0.95}Mg_{0.05}O$ and $Zn_{0.90}Mg_{0.10}O$ was similar; this is because the catalyst had the same amount of surface area and defect concentrations. In this study, Mg-doped ZnO nanostructures showed a larger efficiency for photocatalytic degradation compared to the

La-doped ZnO nanostructures although the Mg-doped ZnO nanostructures had a less specific surface area than the La-doped ZnO nanostructures. This again might result from the differences in particle shape [36,37].

The photocatalytic degradation of MB catalyzed by the La- and Mg-doped ZnO nanostructures fitted a pseudo first-order reaction as shown in Fig. 10 according to the relationship as follows [13].

$$-\frac{dC}{dt} = Kt \quad \text{or} \quad \ln\left(\frac{C_0}{C}\right) = Kt \tag{7}$$

where C_0 is the initial concentration of MB, C is the actual concentration of MB, t is the irradiation time and K is the apparent rate constant of the photocatalytic degradation. The apparent rate constants are presented in Table 2. It was evident that the $Zn_{0.95}Mg_{0.05}O$ nanostructures exhibited the largest apparent rate constant and this corresponds to previous results. It was noticeable, that although the $Zn_{0.90}Mg_{0.10}O$ nanostructures had a larger specific surface area than the $Zn_{0.95}Mg_{0.05}O$ nanostructures, the efficiency of photocatalytic degradation of the $Zn_{0.90}Mg_{0.10}O$ nanostructures is smaller. This might be due to the formation of an amorphous MgO on the surface of catalyst and this MgO phase had a larger E_g value (5.4 eV), so it is difficult to excite electrons and caused the reduction of the photocatalytic degradation of MB.

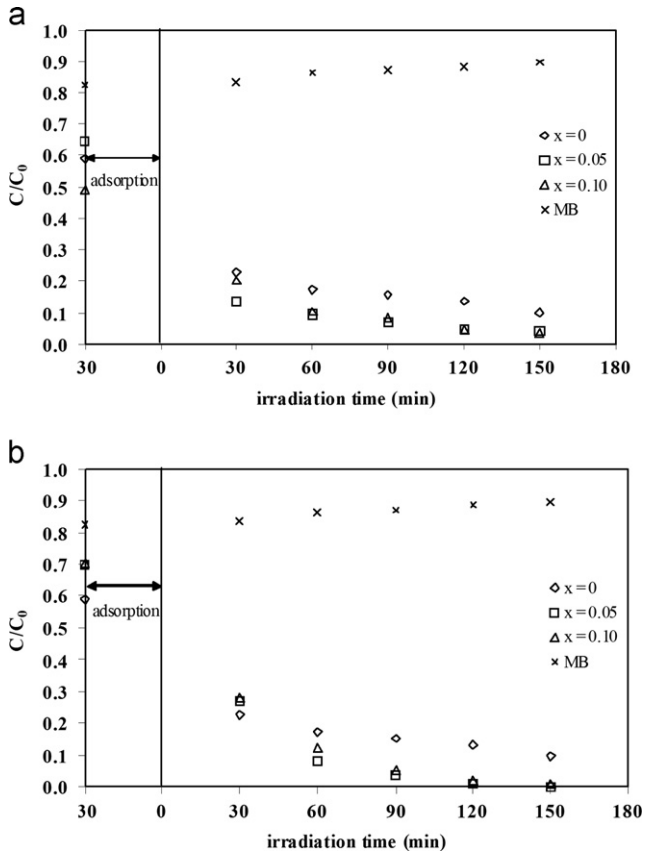

Fig. 9. A comparison of the photocatalytic degradation by the (a) $Zn_{1-x}La_xO$ nanostructure and (b) the $Zn_{1-x}Mg_xO$ nanostructure.

Considering the correlation of rate constant and E_g value, it was evident that the La-doped ZnO nanostructures had lower E_g value than the ZnO nanostructures because of the larger amount of oxygen vacancies. During the photocatalytic process, the electron–hole pairs were generated and the charge carriers were trapped before the recombination of the electrons and holes. This resulted in an increase of the rate constant or enhancement of photocatalytic activity as observing in the Cu-doped ZnO nanoparticles [38]. On the other hand, the rate constant of the Mg-doped ZnO nanostructures was higher than for the ZnO nanostructures. This might be due to the larger E_g value of Mg-doped ZnO nanostructures, thus the electron–hole recombination is reduced (the amount of defect is similar in the case of Mg-doped ZnO nanorods). Therefore, the potocatalytic efficiency enhanced as reported in the case of ZnO nanowires grown by the vapor transport technique [39]. Nevertheless, when the MgO formed and covered the surface of the ZnO nanostructures, the E_g value increased. In addition, the electrons in the valence band cannot be excited and transferred to the conduction band when the E_g value is too high because the tube efficiency emits UV at 315–400 nm only. Therefore, in this study the photocatalytic degradation for $Zn_{0.90}Mg_{0.10}O$ decreased.

The photocatalytic mechanism for ZnO can be expressed by the following reactions [40].

$$ZnO + h\nu \rightarrow ZnO\left(h^+_{vb} + e^-_{cb}\right)$$

$$h^+_{vb} + H_2O \rightarrow {}^{\bullet}OH + H^+$$

Table 2
The photocatalytic and antibacterial activities of $Zn_{1-x}La_xO$ and $Zn_{1-x}Mg_xO$ nanostructures.

Dopant	Content (x)	Surface area (m^2/g)	k (min^{-1})	R^2	MIC (mg/mL)	
					S. aureus	*E. coli*
La	0	11.62	0.0064	0.9713	12.5	–
	0.05	29.89	0.0161	0.9842	3.125	25
	0.10	27.52	0.0147	0.9733	6.25	25
Mg	0	11.62	0.0064	0.9713	12.5	–
	0.05	19.02	0.0440	0.9666	6.25	25
	0.10	19.66	0.0285	0.9993	0.78	25

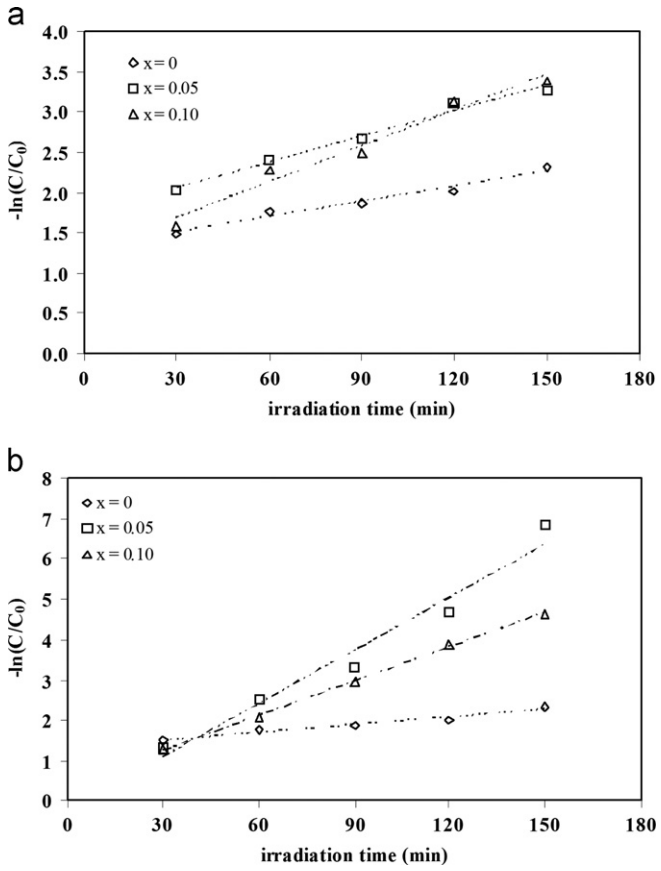

Fig. 10. Kinetic studies of the photocatalytic degradation of the MB solution by (a) the $Zn_{1-x}La_xO$ nanostructure and (b) the $Zn_{1-x}Mg_xO$ nanostructure.

$$e^-_{cb} + O_2 \rightarrow \ \bullet O_2^-$$

$$\bullet O_2^- + H_2O \rightarrow H_2O_2 \rightarrow 2\,\bullet OH$$

$$\bullet OH + MB \rightarrow MB_{ox} \rightarrow \text{intermediates} \rightarrow CO_2 + H_2O$$

3.5. Antibacterial activities

The MIC values of the representative samples against *S. aureus* and *E. coli* are presented in Table 2. Each sample exhibited better antibacterial activity against *S. aureus* than *E. coli*. Pure ZnO nanostructures were only active against *S. aureus* and both La- and Mg-doped ZnO nanostructures were also active against *S. aureus* at lower concentrations. This is because of the differences in cell wall structure, cell physiology, metabolism or degree of contact [41]. Up to the present time, it is difficult to identify which of the antibacterial mechanism operate in the dark. Hirota et al. [42] proposed that the antibacterial mechanism in the dark comes from the super-oxide anion radical ($\bullet O_2^-$) that is produced from the surface of the samples. It is well known that the super-oxide anion radicals are highly reactive oxygen species that can create oxidative stress in the cellular system. When the generated super-oxide anion radicals overwhelmed the levels of the cellular antioxidant defense system, it brought about a state of oxidative stress, thereby leading to cell damage [43]. As we know, protein in the cell wall of *S. aureus* and *E. coli* contains many peptide linkages. So, when the super-oxide anion radical attacks the carbonyl carbon atom in the peptide linkages, eventually, the bacteria are destroyed. In this study, the destructive efficiency on the bacteria depended upon the surface area and the presence of oxygen vacancies. The samples that had a higher surface area and oxygen vacancies produced more super-oxide anion radicals, that resulted in a better destruction of bacteria [44]. This result corresponded to those for the efficiency of photocatalytic degradation. An exception, to the case of $Zn_{0.90}Mg_{0.10}O$ nanostructures, was that *S. aureus* were the most sensitive organism, this might be due to the formation of a small MgO phase, but this cannot be detected by the XRD used [12] and this MgO nanoparticle supported the antibacterial mechanism. However, some research workers [45,46] reported that ZnO itself can inhibit *E. coli*, but in this work ZnO did not inhibit the *E. coli*. This might be due to the differences in the amount of reactive oxygen species on the ZnO surface and the differences in the particle size.

As we know, many articles [45,47] have reported that the ZnO nanostructures can be used not only as antibacterial agent, but also as potential anti-cancer agents. Therefore, the influence of the metal-doped ZnO nanostructures toward anti-cancer agent should be studied in detail in the near future because this might be another good candidate for an anti-cancer agent.

4. Conclusions

$Zn_{1-x}La_xO$ and $Zn_{1-x}Mg_xO$ ($x=0-0.10$) nanostructures were successfully synthesized by a sol–gel method. The nanostructured powders were structurally and thermally characterized by XRD, SEM, TEM and TG–DTA, respectively. The La-doped ZnO nanostructures had a spherical shape while the shape of Mg-doped ZnO nanostructures altered from spherical to nanorod as the Mg concentration increased. The crystallite size of the ZnO nanostructures decreased as the doping concentration was increased to $x=0.05$ and the crystallite size increased with a further increase of the doping concentration. These results can be explained by the Zener pinning effect. Under certain conditions, only Mg^{2+} can easily substitute into the Zn^{2+} site and form a substitutional solid solution when the Mg concentration was varied between $x=0$ and 0.07, this was confirmed by the reduction of lattice parameters and the lattice volume. The E_g value of the La-doped ZnO nanostructure depended on the defects in the structure while the E_g value of Mg-doped ZnO nanostructure changed because of the crystallite size and particle shape. La and Mg doping metals can improve the photocatalytic activity of MB and a pseudo-first order reaction fitted well with the range of the reaction time.

Moreover, the La and Mg doping metals did enhance the antibacterial activity especially against *S. aureus*.

Acknowledgment

This research is supported by Thailand Research Fund (TRF) under the Contract number MRG5480072 and Prince of Songkla University. The authors would like to be thankful the Center of Excellence for Innovation in Chemistry (PERCH-CIC), Office of the Higher Education Commission, Ministry of Education and the authors would like to acknowledge Dr. Brian Hodgson for assistance with the English.

References

[1] H. Morkoç, Ü. Özgür, in: Zinc Oxide: Fundamentals, Materials and Device Technology, Wiley-VCH Verlag GmbH & Co. KGaA, Weinheim, 2009.
[2] S.M. Sultan, O.D. Clark, T.B. Masaud, Q. Fang, R. Gunn, M.M.A. Hakim, K. Sun, P. Ashburn, H.M.H. Chong, Remote plasma enhanced atomic layer deposition of ZnO for thin film electronic applications, Microelectronic Engineering 97 (2012) 162–165.
[3] Z.L. Wang, Zinc oxide nanostructures: growth, properties and applications, Journal of Physics: Condensed Matter 16 (2004) R829–R858.
[4] S.K. Asl, S.K. Sadrnezhaad, M.K. Rad, The seeding effect on the microstructure and photocatalytic properties of ZnO nano powders, Materials Letters 64 (2010) 1935–1938.
[5] M.G. Nair, M. Nirmala, K. Rekha, A. Anukaliani, Structural, optical, photo catalytic and antibacterial activity of ZnO and Co doped ZnO nanoparticles, Materials Letters 65 (2011) 1797–1800.
[6] S. Suwanboon, P. Amornpitoksuk, A. Sukolrat, Dependence of optical properties on doping metal, crystallite size and defect concentration of M-doped ZnO nanopowders (M=Al, Mg, Ti), Ceramics International 37 (2011) 1359–1365.
[7] Z. Guo, C. Andreazza-Vignolle, P. Andreazza, T. Sauvage, D.X. Zhao, Y.C. Liu, B. Yao, D.Z. Shen, X.W. Fan, Tuning the growth of ZnO nanowires, Physica B 406 (2011) 2200–2205.
[8] S. Suwanboon, Structural and optical properties of nanocrystalline ZnO powder from sol–gel method, ScienceAsia 34 (2008) 31–34.
[9] J.D. Wright, N.A.J.M. Sommerdijk, in: Sol–Gel Materials Chemistry and Applications, CRC Press, New York, 2001.
[10] Z. Han, L. Ren, Z. Cui, C. Chen, H. Pan, J. Chen, Ag/ZnO flower heterostructures as a visible-light driven photocatalyst via surface plasmon resonance, Applied Catalysis B 126 (2012) 298–305.
[11] R. He, R.K. Hocking, T. Tsuzuki, Local structure and photocatalytic property of sol–gel synthesized ZnO doped with transition metal oxides, Journal of Materials Science 47 (2012) 3150–3158.
[12] V. Etacheri, R. Roshan, V. Kumar, Mg-doped ZnO nanoparticles for efficient sunlight-driven photocatalysis, ACS Applied Materials and Interfaces 4 (2012) 2717–2725.
[13] M. Fu, Y. Li, S. Wu, P. Lu, J. Liu, F. Dong, Sol–gel preparation and enhanced photocatalytic performance of Cu-doped ZnO nanoparticles, Applied Surface Science 258 (2011) 1587–1591.
[14] M. Nirmal, A. Anukaliani, Characterization of undoped and Co doped ZnO nanoparticles synthesized by DC thermal plasma method, Physica B 406 (2011) 911–915.
[15] S. Ghosh, V.S. Goudar, K.G. Padmalekha, S.V. Bhat, S.S. Indi, H.N. Vasan, ZnO/Ag nanohybrid: synthesis, characterization, synergistic antibacterial activity and its mechanism, RSC Advances 2 (2012) 930–940.
[16] C. Karunakaran, V. Rajeswari, P. Gomathisankar, Optical, electrical, photocatalytic, and bactericidal properties of microwave synthesized nanocrystalline Ag–ZnO and ZnO, Solid State Sciences 13 (2011) 923–928.
[17] P. Amornpitoksuk, S. Suwanboon, S. Sangkanu, A. Sukhoom, N. Muensit, J. Baltrusaitis, Synthesis, characterization, photocatalytic and antibacterial activities of Ag-doped ZnO powders modified with a diblock copolymer, Powder Technology 219 (2012) 158–164.
[18] K. Rekha, M. Nirmala, M.G. Nair, A. Anukaliani, Structural, optical, photocatalytic and antibacterial activity of zinc oxide and manganese doped zinc oxide nanoparticles, Physica B 405 (2010) 3180–3185.
[19] S.D. Sarker, L. Nahar, Y. Kumarasamy, Microtitre plate-based antibacterial assay incorporating resazurin as an indicator of cell growth, and its application in the *in vitro* antibacterial screening of phytochemicals, Methods 42 (2007) 321–324.
[20] C. Ge, C. Xie, M. Hu, Y. Gui, Z. Bai, D. Zeng, Structural characteristics and UV-light enhanced gas sensitivity of La-doped ZnO nanoparticles, Materials Science and Engineering B 141 (2007) 43–48.
[21] S.S. Alias, A.B. Ismail, A.A. Mohamad, Effect of pH on ZnO nanoparticle properties synthesized by sol–gel centrifugation, Journal of Alloys and Compounds 499 (2010) 231–237.
[22] R. Elilarassi, G. Chandrasekaran, Synthesis, structural and optical characterization of Ni-doped ZnO nanoparticles, Journal of Materials Science: Materials in Electronics 22 (2011) 751–756.
[23] A. Khorsand Zak, W.H.Abd Majid, M.E. Abrishami, R. Yousefi, X-ray analysis of ZnO nanoparticles by Williamson–Hall and size–strain plot methods, Solid State Sciences 13 (2011) 251–256.
[24] W. Smith, J. Hashemi, Foundation of Material Science and Engineering, McGrawHill, New York, 2006.
[25] S. Anandan, A. Vinu, K.L.P. Sheeja Lovely, N. Gokulakrishnan, P. Srinivasu, T. Mori, V. Murugesan, V. Sivamurugan, K. Ariga, Photocatalytic activity of La-doped ZnO for the degradation of monocrotophos in aqueous suspension, Journal of Molecular Catalysis A: Chemical 266 (2007) 149–157.
[26] T.M. Hammad, J.K. Salem, Synthesis and characterization of Mg-doped ZnO hollow spheres, Journal of Nanoparticle Research 13 (2011) 2205–2212.
[27] T. Dhannia, S. Jayalekshmi, M.C.S. Kumar, T.P. Rao, A.C. Bose, Effect of iron doping and annealing on structural and optical properties of cerium oxide nanocrystals, Journal of Physics and Chemistry of Solids 71 (2010) 1020–1025.
[28] M. Farbod, M.Z. Shoushtari, S. Parhoodeh, Fabrication and characterization of $Zn_{1-x}Al_xO$ nanoparticles by DC arc plasma, Physica B 406 (2011) 205–210.
[29] L. Yanmei, W. Tao, S. Xia, F. Qingqing, L. Qingrong, S. Xueping, S. Zaoqi, Structural and photoluminescent properties of Ni doped ZnO nanorod arrays prepared by hydrothermal method, Applied Surface Science 257 (2011) 6540–6545.
[30] F.K. Masoud, F. Zeinab, R.L.E. Mohammad, S.R. Reza, Different morphologies of ZnO nanostructures via polymeric complex sol–gel method: synthesis and characterization, Journal of Sol–Gel Science and Technology 64 (2012) 193–199.
[31] F. Ejehi, S.P.H. Marashi, M.R. Ghaani, D.F. Haghshenas, The synthesis of NaSICON-type $ZrNb(PO_4)_3$ structure by the use of Pechini method, Ceramics International 38 (2012) 6857–6863.
[32] M. Vafaee, M.S. Ghamsari, S. Radiman, Highly concentrated zinc oxide nanocrystals sol with strong blue emission, Journal of Luminescence 131 (2011) 155–158.
[33] P. Amornpitoksuk, S. Suwanboon, S. Sangkanu, A. Sukhoom, J. Wudtipan, K. Srijan, S. Kaewtaro, Synthesis, photocatalytic and antibacterial activities of ZnO particles modified by diblock copolymer, Powder Technology 212 (2011) 432–438.
[34] S. Suwanboon, P. Amornpitoksuk, N. Muensit, Dependence of photocatalytic activity on structural and optical properties of nanocrystalline ZnO powders, Ceramics International 37 (2011) 2247–2253.
[35] S. Suwanboon, P. Amornpitoksuk, A. Sukolra, N. Muensit Optical and photocatalytic properties of La-doped ZnO nanoparticles prepared via

precipitation and mechanical milling method, Ceramics International http://dx.doi.org/10.1016/j.ceramint.2012.09.050, in press.
[36] D. Li, H. Haneda, Morphologies of zinc oxide particles and their effects on photocatalysis, Chemosphere 51 (2003) 129–137.
[37] L. Song, S. Zhang, X. Wu, Q. Wei, Controllable synthesis of hexagonal, bullet-like ZnO microstructures and nanorod arrays and their photocatalytic property, Industrial & Engineering Chemistry Research 51 (2012) 4922–4926.
[38] R. Mohan, K. Krishnamoorthy, S.J. Kim, Enhanced photocatalytic activity of Cu-doped ZnO nanorods, Solid State Communications 152 (2012) 375–380.
[39] R. Mohan, K. Krishnamoorthy, S.J. Kim, Diameter dependent photocatalytic activity of ZnO nanowires grown by vapor transport technique, Chemical Physics Letters 539–540 (2012) 83–88.
[40] P. Amornpitoksuk, S. Suwanboon, S. Sangkanu, A. Sukhoom, N. Muensit, Morphology, photocatalytic and antibacterial activities of radial spherical ZnO nanorods controlled with a diblock copolymer, Superlattices and Microstructures 51 (2012) 103–113.
[41] Z. Emami-Karvani, P. Chehrazi, Antibacterial activity of ZnO nanoparticle on gram-positive and gram-negative bacteria, African Journal of Microbiology Research 5 (2011) 1368–1373.
[42] K. Hirota, M. Sugimoto, M. Kato, K. Tsukagoshi, T. Tanigawa, H. Sugimoto, Preparation of zinc oxide ceramics with a sustainable antibacterial activity under dark conditions, Ceramics International 36 (2010) 497–506.
[43] K. Krishnamoorthy, J.Y. Moon, H.B. Hyun, S.K. Cho, S.J. Kim, Mechanistic investigation on the toxicity of MgO nanoparticles toward cancer cells, Journal of Materials Chemistry 22 (2012) 24610–24617.
[44] K. Krishnamoorthy, G. Manivannan, S.J. Kim, K. Jeyasubramanian, M. Premanathan, Antibacterial activity of MgO nanoparticles based on lipid peroxidation by oxygen vacancy, Journal of Nanoparticle Research 14 (2012) 1–10.
[45] M. Premanathan, K. Krishnamoorthy, K. Jeyasubramanian, G. Manivannan, Selective toxicity of ZnO nanoparticles toward gram-positive bacteria and cancer cells by apoptosis through lipid peroxidation, Nanomedicine: Nanotechnology, Biology and Medicine 7 (2011) 184–192.
[46] Y. Liu, L. He, A. Mustapha, H. Li, Z.Q. Hu, M. Lin, Antibacterial activities of zinc oxide nanoparticles against *Escherichia coli* O157:H7, Journal of Applied Microbiology 107 (2009) 1193–1201.
[47] M. Ahamed, M.J. Akhtar, M. Raja, I. Ahmad, M. Kaleem, J. Siddiqui, M.S. AlSalhi, S.A. Alrokayan, ZnO nanorod-induced apoptosis in human alveolar adenocarcinoma cells via p53, surviving and bax/bcl-2 pathways: role of oxidative stress, Nanomedicine: Nanotechnology, Biology and Medicine 7 (2011) 904–913.